Journal of Catalysis 315 (2014) 48–58

Contents lists available at ScienceDirect

Journal of Catalysis

journal homepage: www.elsevier.com/locate/jcat

Acid strength and bifunctional catalytic behavior of alloys comprised of noble metals and oxophilic metal promoters

David Hibbitts [a,1], Qiaohua Tan [a], Matthew Neurock [a,b,*]

[a] Department of Chemical Engineering, University of Virginia, Charlottesville, VA 22904, United States
[b] Department of Chemistry, University of Virginia, Charlottesville, VA 22904, United States

ARTICLE INFO

Article history:
Received 6 September 2013
Revised 12 March 2014
Accepted 31 March 2014
Available online 21 May 2014

Keywords:
Hydrogenolysis
Ring opening cyclic ethers
DFT, bifunctional catalysis
Hydrodeoxygenation
Oxophilic metal promoters
Deprotonation energies
Hydroxymethyl tetrahydrofuran

ABSTRACT

The promotion of metal catalysts with partially oxidized oxophilic MO_x species, such as ReO_x-promoted Rh, has been demonstrated to produce Brønsted acid sites that can promote hydrogenolysis of oxygenate intermediates such as those found in biomass-derived species. A wide variety of alloy compositions and structures are examined in this work to investigate strongly acidic promoters by using DFT-calculated deprotonation energies (DPE) as a measure of acid strength. Sites with the highest acid strength had DPE less than 1100 kJ mol^{-1}, similar to DPE values of heteropolyacids or acid-containing zeolites, and were found on alloys composed of an oxophilic metal (such as Re or W) with a noble metal (such as Rh or Pt). NH_3 adsorbs more strongly to sites with increasing acid strength and the activation barriers for acid-catalyzed ring opening of a furan ring decrease with increasing acid strength, which was also shown to be stronger for OH acid sites bound to multiple oxophilic metal atoms in a three-fold configuration rather than OH sites adsorbed in an atop configuration on one oxophilic metal, indicating that small MO_x clusters may yield sites with the highest acid strength.

1. Introduction

Biomass, which is comprised of carbohydrates that can be hydrolyzed to form C_5–C_6 sugars rich in oxygen, provides a sustainable alternative to petroleum for the production of fuels and chemicals but requires efficient strategies to selectively remove oxygen. Various heterogeneous-catalyzed paths, which include decarboxylation, decarbonylation, and hydrogenolysis, have been proposed and used to selectively produce value-added chemicals as well as intermediates with higher H/C ratios for fuel production [1–3]. Among these paths, hydrogenolysis has the distinct advantage of maintaining the chain length of the hydrocarbon substrate, thus avoiding the unnecessary production of CO or CO_2 by-products and providing a carbon neutral process.

Hydrogenolysis of various polyols, including glycerol, a by-product of biodiesel production [1], has been targeted in the literature for synthesis of valuable chemical intermediates or fuel precursors. Glycerol hydrogenolysis is active over various supported metal catalysts, including Ru [4–7], Pd [4,8], Pt [4,6,9], Rh [8,10], and PtRu and AuRu [6] alloys at temperatures near 473 K under moderate pressures of hydrogen (14–100 bar). Carbon-supported Pt, Pd, and Rh catalysts predominantly convert glycerol via C–O hydrogenolysis to *1,2-propanediol (1,2-PrDO)* with ~80% initial selectivity [4,6,8,9], which undergoes further C–O hydrogenolysis to form propanol; these catalysts, however, also show activity for C–C hydrogenolysis, leading to undesired C_2 products. Chia et al. recently examined the hydrogenolysis of glycerol on Rh/C catalysts at a lower temperature (393 K) and found that C–C hydrogenolysis was suppressed resulting in a product distribution of 18% *1,2-PrDO*, 5% *1,3-PrDO*, 8% 1-propanol (*1-PrOH*), and 69% 2-propanol (*2-PrOH*) [11]. These product selectivities indicate that the C–O hydrogenolysis of glycerol primarily occurs at the less-substituted (terminal) carbon center on these metal catalysts.

Cyclic ethers derived from biomass [3,12] such as 2-(hydroxymethyl)tetrahydrofuran (*HMTHF*) can also undergo C–O hydrogenolysis, opening their ring to form linear or branched products. The ability to selectively activate specific C–O bonds in the ring could result in sustainable routes to valuable chemical intermediates. Work on Rh/SiO_2 has indicated that C–O hydrogenolysis occurs more selectively at the unsubstituted carbon of the ring-ether, forming *1,2-pentanediol* (*1,2-PeDO*) at >60% selectivity [13].

In addition to these unpromoted catalysts, a number of studies over supported noble metal catalysts such as Rh, Pt, and Ir promoted by acidic species or substrates such as amberlyst [14–16],

* Corresponding author at: Department of Chemical Engineering, University of Virginia, Charlottesville, VA 22904, United States. Fax: +1 434 982 2658.
E-mail address: mn4n@virginia.edu (M. Neurock).
[1] Present address: Department of Chemical and Biomolecular Engineering, University of California, Berkeley, CA 94720, United States.

http://dx.doi.org/10.1016/j.jcat.2014.03.016
0021-9517/

H_2SO_4 [17,18], H_2WO_4 [8,15], and $H_4SiW_{12}O_{40}$ [19] or alloyed with partially reduced oxides such as MoO_x [10,11,20,21], WO_x [10,20], or ReO_x [10,13,18,20–23] have demonstrated distinctly different trends in selectivity as C–O hydrogenolysis predominantly proceeds at the *more* substituted C–O bonds. *HMTHF* preferentially opens at the more substituted C–O bond to form 1,5-pentanediol with greater than 95% selectivity in the presence of these promoters, and similar results were observed for C_6 cyclic ethers [11,13,20,21]. For glycerol, these promoters result in significant increases in the selectivity to *1,3-PrDO* [9–11,18,23] which is only observed in small quantities on the unpromoted catalysts and at higher temperatures. ReO_x on Pt, for example, was shown to significantly increase the rate of glycerol reforming compared to that on unpromoted Pt [24,25]. Chia et al. studied hydrogenolysis of a wide range of polyols in addition to glycerol and *HMTHF* over ReO_x-promoted Rh/C and observed that hydrogenolysis selectively occurs at secondary alcohol groups [11]. Koso et al. later reported similar results for hydrogenolysis of many of the same polyols over ReO_x and MoO_x-promoted Rh/SiO_2 [21]. We showed previously that rates and selectivities for hydrogenolysis of a wide range of linear polyols and C_5 and C_6 ethers could be linearly related to their gas-phase carbenium ion reaction energies [11], thus indicating that ReO_x, WO_x, and MoO_x promoters result in the formation of acid sites which are likely M-OH groups at the metal–solution interface.

Although the specific nature of the active acid site is unknown, these sites are thought to be either embedded into or strongly bound to the promoted metal as the presence of acids in solution such as H_2SO_4 or HCl is far less active and selective and cannot maintain the sustained operational times (>120 h) demonstrated for ReO_x-Rh/SiO_2 [11]. NH_3 TPD offers experimental evidence of acid sites on ReO_x-promoted Pt/C and that the acid site density, but not strength, increases with Re loading [25]. The ratio of acid to metal sites is 0.28 for a Re:Rh loading of 1:2 with an NH_3 adsorption energy on the acid site of −100 kJ/mol, indicating moderate acid strength [11]. EXAFS has been performed on a number of these alloys, including Rh-ReO_x [10,13,21,26], Rh-MoO_x [21], Pt-ReO_x [9,27], and most recently, Ir-ReO_x [18] and curve-fitting results from these studies offer insights into the nature of the alloy and therefore the acid site, however, large uncertainties weaken the conclusions one can draw.

First-principle density functional theory (DFT) calculations can be used to examine and test acid strength of possible sites for a wide range of alloy materials as previously reported [11]. The deprotonation energy (DPE) provides a direct measure of acid site strength [28] and was used to examine acid strength of hydroxylated Re in the surface of 201-atom cubo-octahedral Rh and Pt nanoparticles as well as other alloys. The results indicate that materials such as ReO_x-promoted Rh have DPE values that are similar to those for heteropolyacids (HPAs) such as $H_4SiW_{12}O_{40}$ [19,28]. We extend these preliminary ideas in this work by systematically examining a wider range of acid sites that can form in different alloys and evaluating the role of O–H bond strength and EA of the resulting conjugate base. Furthermore, we seek to determine how DPE compares with experimentally-relevant measurements such as the NH_3 adsorption energy as well as ring-opening reactivity.

2. Computational methodology

First-principle DFT calculations were carried out to determine all of adsorption, reaction, and activation energies reported herein over both ideal single crystal (1 1 1) surfaces and 201-atom cubo-octahedral metal clusters using the Vienna ab initio simulation package (VASP) [29–31]. Planewaves were constructed with an energy cutoff of 396 eV and Vanderbilt ultrasoft pseudopotentials with real space projection operators defining the features of the core region. The correlation and exchange energies were obtained using the Perdew–Wang 91 (PW91) form of the generalized gradient approximation (GGA) [32].

Vacuum-phase calculations were performed spin-polarized using an $18 \times 18 \times 18$ Å unit cell. Ideal single crystal surfaces were modeled as two-dimensional slabs with a 3×3 unit cell and 4 metal layers in the *z*-direction. Slabs were separated by 10 Å and the bottom two layers were held fixed in their bulk atomic positions while the top two layers were allowed to fully relax. Calculations on surfaces were carried out non-spin-polarized until the maximum force upon any atom was less than 0.05 eV/Å; forces were obtained using a fast Fourier transform (FFT) grid with a cutoff of twice the planewave cutoff; wavefunctions were converged to within 10^{-6} eV with a $3 \times 3 \times 1$ *k*-point mesh. Once the geometry was converged, a single-point calculation is performed at a $6 \times 6 \times 1$ *k*-point mesh.

Transition state calculations for ring opening of *HMTHF* were carried out by first determining the minimum energy path (MEP) using the NEB method [33,34] with 8–16 images converged to 0.3 eV/Å to generate initial structures for simulations that use the Dimer method [35] and are run with the same level of accuracy as the optimizations described above. The transition states were verified on a selected number of systems by carrying out a full normal mode analyses. The work function of the metal surfaces was calculated as the difference between the Fermi energy and the maximum *xy*-averaged potential, which is within the vacuum region separating the periodic slabs.

Metal particles were modeled using 201-atom cubo-octahedral particles shown in Fig. 1. Calculations on metal particles were carried non-spin-polarized in a cubic unit cell with a minimum of 12 Å of vacuum separating particles between periodic cells. All structure optimizations reported were carried out until the maximum force upon any atom was less than 0.05 eV/Å; forces were obtained using a fast Fourier transform (FFT) grid with a cutoff of twice the planewave cutoff; wavefunctions were converged to within 10^{-6} eV. These calculations were performed using the γ-point version of VASP. Monopole and dipole moments of the cell were calculated and used to correct the energy; for charged calculations, quadrupole corrections were also applied. The effect of tighter convergence criteria was negligible on the quantities calculated below, as shown in Table S1. The work function was calculated as the difference between the Fermi energy and the *xy*-averaged potential at the point $z = 0$, which is within the vacuum region separating the periodic clusters.

Deprotonation energy (DPE) is defined as the energy difference between the MOH of the cluster/surface and the separated anionic cluster/surface and the H + species (Eq. (1)). Dehydrogenation energy (DHE) is defined as the energy difference between homolytically dissociated ($MO^{\cdot} + H^{\cdot}$) and initial MOH states (Eq. (2)). Electron affinity of the conjugate base (EA) is defined as the negative of the change in energy upon charging the neutral MO site for an extra electron (Eq. (3)). Eqs. (1)–(3) can be rearranged in order to show the direct relationship between DPE, DHE, and EA (Eq. (4)). Alternatively, rather than explicitly calculating charged systems, the work function (WF) of the $MO_{\cdot}$ system can be used to compute the DPE (DPE^{WF}, Eq. (5)); for bulk metals, the WF is essentially equivalent to the negative of electron affinity (EA); however, as discussed below, this is not the case for small 201-atom particles as a result of the small band gaps for finite-sized metal clusters. NH_3 adsorption energies (NH_3 AE) were calculated as the energy difference between the bound state and the MOH cluster plus the energy of NH_3 in a vacuum cell (Eq. (6)). Binding energies (BE) of O^* and OH^* were calculated as the energy differences between the bound state and the metal cluster plus the energy of the $O^{\cdot}$ or $OH^{\cdot}$ in a vacuum cell (Eqs. (7) and (8)). Eq. (9) shows

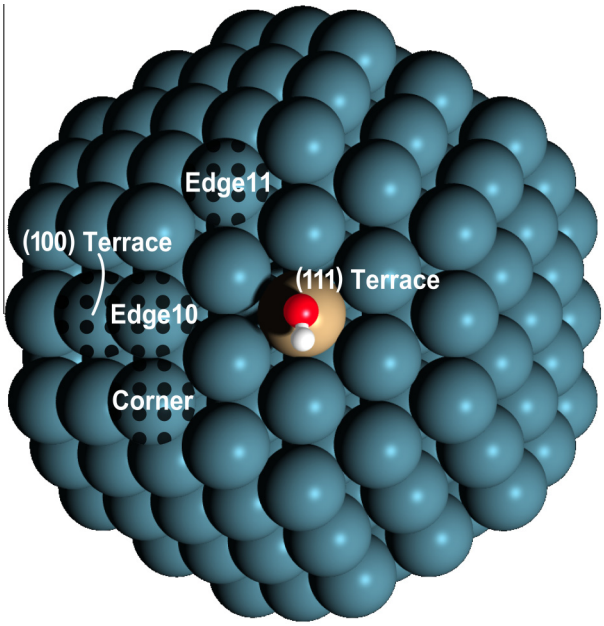

Fig. 1. Hydroxylated (111) terrace surface monoalloy site. Dotted atoms represent the (100) terrace, edge11, edge10 and corner sites.

the rearrangement of Eqs. (2), (7), and (8) to show the relationship between the DHE and the binding energies of O^* and OH^*. Conventions used herein define a lower DPE as a higher acid strength, a lower DHE as a weaker O–H bond, and more negative NH_3, O^* and OH^* binding energies as stronger adsorption strengths.

$$DPE = E[MO^-] + E[H^+] - E[MOH] \quad (1)$$

$$DHE = E[MO\cdot] + E[H\cdot] - E[MOH] \quad (2)$$

$$EA = -(E[MO^-] - E[MO\cdot]) \quad (3)$$

$$DPE = DHE + EA + (E[H^+] - E[H\cdot]) \quad (4)$$

$$DPE^{WF} = DHE - WF + (E[H+] - E[H\cdot]) \quad (5)$$

$$NH_3AE = E[MOH - NH_3] - E[MOH] - E[NH_3] \quad (6)$$

$$OBE = E[MO] - E[M] - E[O\cdot] \quad (7)$$

$$OH\ BE = E[MOH] - E[M] - E[OH\cdot] \quad (8)$$

$$DHE = O\ BE - OH\ BE - (E[OH\cdot] - E[O\cdot] - E[H\cdot]) \quad (9)$$

3. Results and discussion

A series of calculations were performed on alloys of different compositions, varying the location of the MOH site on the nanoparticle. The energies required to determine DPE values and the NH_3 adsorption energies outlined in Eqs. (1)–(8) and shown in the Born Haber cylces in Fig. S1 in the Supporting Information (SI) were calculated on each of the alloy structures examined. These data are used to establish trends between these features, such as the NH_3 AE and the DPE. Ring-opening reactions of *HMTHF* were then studied on a (111) surface of each alloy composition to determine the relationship between activation barriers for this acid-catalyzed reaction on acid site characteristics. For ReO_x-promoted Rh, an additional set of calculations is presented, which demonstrates the effect of the structure of the alloy site on the DPE, NH_3 AE, and other characteristics.

3.1. Effect of alloy composition and site on DPE

O^* and OH^* BE, NH_3 AE, DHE, and DPE were calculated on the Pt_{201}, Rh_{201}, Au_{201}, Ir_{201}, and Ru_{201} clusters alloyed with single metal atom promoters (Pt, Mo, Ru, W, and Re) within the surface layer (in-surface monoalloy sites). The results reported in Table 1 examine in detail five different metal atom sites for the substitution of the promoter in the 201 atom cubo-octahedral cluster including a (111) terrace, a (100) terrace, an edge between two (111) surfaces (edge 11), an edge between a (111) and (100) surface (edge 10), and a corner site for Pt–Re and Rh–Re clusters; these sites are highlighted in Fig. 1. For the other alloys, only the sites with the lowest DPE values (highest acid strength) are shown in Table 1. All of the other sites were calculated and are presented in Tables S2–S6 and their values are included in subsequent Figs. 2–4. DPE values for all of particles examined range from 1065 kJ mol^{-1} for ReO_x-promoted Pt to 1345 kJ mol^{-1} for monometallic Au as can be seen in Table 1 which cover the range of highly acidic to non-acidic sites.

The DPE of a particular site can be deconstructed using a Born–Haber cycle (Eq. (4)) and written as the summation of energies for the elementary thermochemical steps that comprise the deprotonation process: dehydrogenation energy (DHE) of the M–OH ($MOH \rightarrow MO + H$), ionization energy of the hydrogen atom ($H \rightarrow H^+ + e^-$) which is constant, and electron affinity (EA) of the metal cluster ($MO + e^- \rightarrow MO^-$). The results presented in Table 1 indicate that EA depends only upon the "bulk" metal and does not vary appreciably with site or composition of the alloyed element since EA is a bulk property and these models only have one alloyed site within the entire 201-atom cluster. Rather than explicitly calculating the EA, it can be inferred instead from the WF of the metal particle, leading to a different DPE values (DPE^{WF}). Fig. S2 shows the linear relationship between EA and WF resulting in DPE^{WF} being lower than DPE by a nearly constant value of 74 kJ mol^{-1}, which relates to the difference between EA and WF of these 201-atom particles which decreases with increasing particle size (Fig. S3). Ultimately, this indicates that the choice of computing DPE from the WF or the EA only shifts the absolute values of DPE and does not change any of trends discussed. Since EA is constant for each "bulk" metal and the value for ($E[H^+] - E[H]$) is independent of the catalyst (Eq. (4)), there is a direct linear relationship between DPE and DHE, as shown in Fig. 2a, where the slope for each line is equal to 1 and the *y*-intercept depends upon EA which follows the following trend: Ru > Rh > Au > Ir > Pt. DHE depends on both the site and the alloy composition and a site with a low DHE is desired to generate a stronger acid site (lower DPE) and requires a weakly bound hydroxyl and a strongly bound oxygen atom at the promoter site as shown in Eq. (8); sites such as these are shown in the upper-left-hand portion of Fig. 2b.

Bond-order conservation would indicate that increasing the strength of the M–O bond will decrease the strength of the O–H bond as the result of a competition between the two bonds over the valence electrons of the oxygen atom. In order to increase the M–O bond strength, either the strength or number of M–M bonds must change at the OH^* site. In this work, we analyze the effects of decreasing the number of M–M bonds by examining sites with different metal coordination numbers. A weak trend exists between the strength of the O–H bond and the CN of the MOH site, as further discussed in the SI (Figs. S4–S6).

Experimental results [11,20] have shown that ReO_x-promoted Rh catalysts are more active than MoO_x-promoted Rh catalysts, consistent with DFT-calculated DPE values for ReOx-promoted Rh (1150 kJ mol^{-1}) being lower than MoOx-promoted Rh (1177 kJ mol^{-1}) as shown in Fig. 3, indicating an increase in activity with increasing acid strength. Experimental results suggest that promoted Rh is more active than promoted Pt, followed by

Table 1
Selected results from in-surface monoalloy sites.

Bulk	Alloy	Site	CN	O BE (kJ mol^{-1})	OH BE (kJ mol^{-1})	NH_3 AE (kJ mol^{-1})	DHE (kJ mol^{-1})	EA (kJ mol^{-1})	WF (kJ mol^{-1})	DPE (kJ mol^{-1})	DPE^{WF} (kJ mol^{-1})	MOH-NH_3 bond lengths M–O (Å)	O–H (Å)	H–N (Å)
Pt	**Pt**	*corner*	6	−338	−258	−40	364	454	529	1227	1152	1.92	1.02	1.67
	Mo	*111 terrace*	9	−537	−326	−95	233	451	525	1099	1025	1.76	1.49	1.10
	Ru	*corner*	6	−529	−345	−59	260	452	526	1124	1050	1.84	1.06	1.55
	W	*111 terrace*	9	−577	−360	−104	228	451	525	1093	1019	1.75	1.50	1.09
	Re	*111 terrace*	9	−549	−329	−88	224	450	524	1091	1017	1.76	1.50	1.09
		100 terrace	8	−560	−356	−87	240	451	524	1106	1033	1.78	1.52	1.09
		edge11	7	−630	−400	−95	215	452	526	1079	1033	1.77	1.44	1.11
		edge10	7	−642	−416	−107	219	451	525	1084	1068	1.76	1.50	1.09
		corner	6	−702	−458	−102	201	452	526	1065	991	1.76	1.45	1.11
Rh	**Rh**	*corner*	6	−414	−297	−36	327	392	467	1251	1176	1.90	1.02	1.72
	Mo	*111 terrace*	9	−536	−325	−71	233	389	464	1161	1086	1.79	1.44	1.12
	Ru	*corner*	6	−531	−355	−45	269	391	466	1194	1119	1.86	1.03	1.63
	W	*111 terrace*	9	−576	−356	−82	224	389	465	1152	1076	1.77	1.47	1.11
	Re	*111 terrace*	9	−542	−314	−71	216	388	463	1145	1070	1.85	1.13	1.40
		100 terrace	8	−556	−349	−48	238	388	462	1166	1092	1.88	1.05	1.61
		edge11	7	−611	−386	−69	219	390	465	1146	1071	1.78	1.54	1.09
		edge10	7	−630	−405	−69	220	389	464	1147	1072	1.83	1.12	1.42
		corner	6	−676	−451	−70	220	391	466	1145	1070	1.81	1.11	1.40
Au	**Au**	*100 terrace*	8	−195	−188	−28	437	409	483	1345	1284	2.05	1.00	1.91
	Mo	*corner*	6	−732	−473	−86	186	407	478	1096	1025	1.77	1.40	1.13
	Ru	*corner*	6	−529	−341	−47	257	407	478	1167	1096	1.84	1.05	1.59
	W	*edge10*	7	−715	−434	−105	164	407	479	1073	1002	1.74	1.48	1.11
	Re	*corner*	6	−744	−461	−95	162	406	477	1072	1001	1.74	1.47	1.10
Ir	**Ir**	*corner*	6	−492	−332	−53	285	432	506	1169	1095	1.88	1.04	1.60
	Mo	*111 terrace*	9	−524	−319	−89	239	431	505	1125	1051	1.77	1.42	1.12
	Ru	*corner*	6	−519	−349	−55	274	432	506	1159	1085	1.84	1.06	1.52
	W	*111 terrace*	9	−570	−354	−102	229	431	506	1114	1040	1.75	1.49	1.10
	Re	*111 terrace*	9	−527	−300	−93	217	430	504	1103	1030	1.74	1.54	1.08
Ru	**Ru**	*corner*	6	−526	−356	−42	275	371	446	1220	1146	1.88	1.01	1.79
	Mo	*111 terrace*	9	−552	−348	−64	240	369	444	1188	1113	1.83	1.09	1.46
	W	*111 terrace*	9	−597	−378	−76	225	369	444	1173	1098	1.77	1.46	1.11
	Re	*111 terrace*	9	−552	−319	−73	211	369	443	1159	1085	1.76	1.49	1.10

Full set of calculated results are given in the Supplemental Information, Table S2–S6.

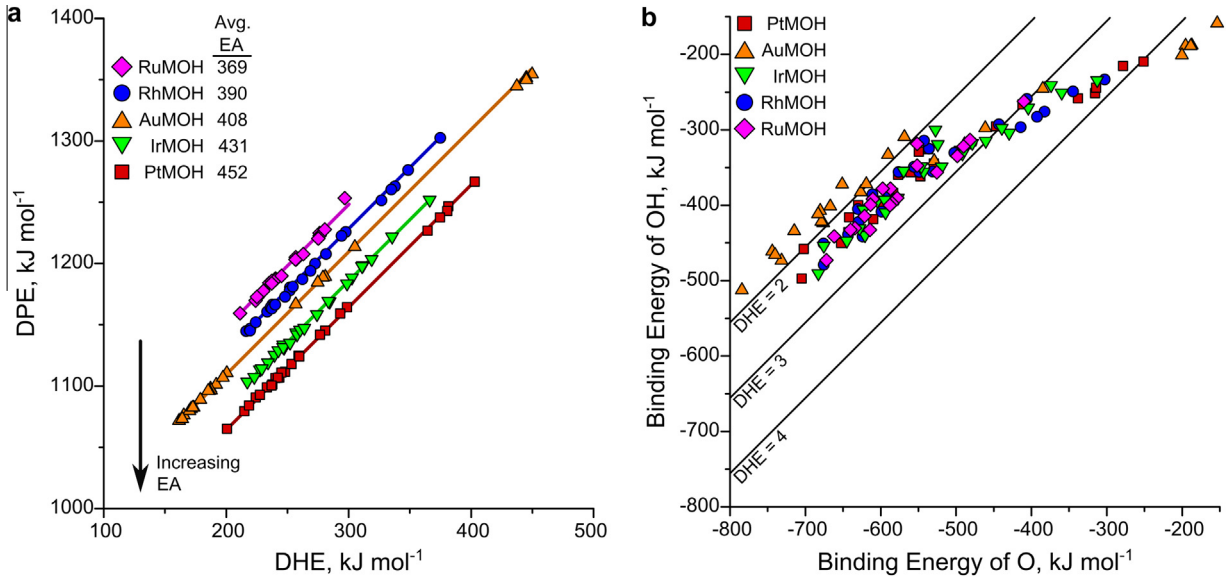

Fig. 2. (a) (Left) DPE is linearly proportional to DHE with a slope of 1 and the *y*-intercept shifted by the EA of the 'bulk' metal. (b) (Right) DHE shown as the relationship between the BE of O* and OH*. The O* and OH* binding energies both increase in the same manner. The slope of this curve, however, is <1, indicating that stronger O* will have lower DHE, indicating weaker O–H bonds.

promoted Ir [9–11]. These differences in activity of the bulk metals, however, are not consistent with the calculated differences in DPE of these bulk metals reported herein. The experimental rates, however, have not been normalized by the number of acid sites present on the promoted catalyst. The number of acid sites has been estimated through NH_3 TPD for ReO_x-promoted Rh [11], but no such

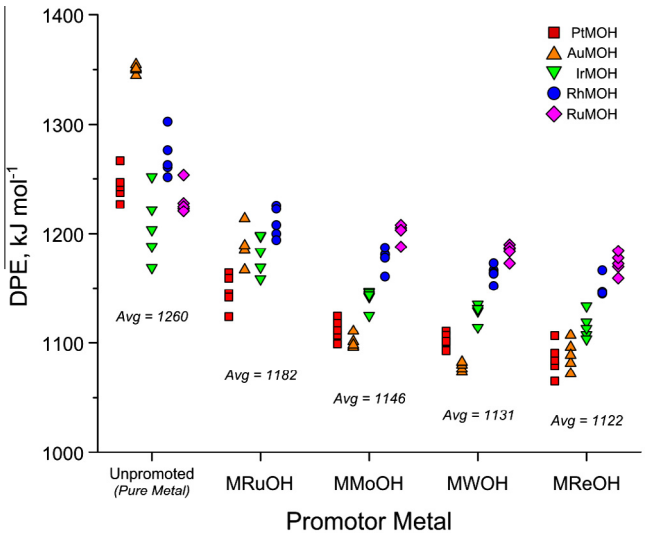

Fig. 3. DPE of in-surface alloys of various compositions. On average, Re-promoted nanoparticles appear to have the lowest (highest acid strength) DPE, followed by W, Mo and Ru promoters.

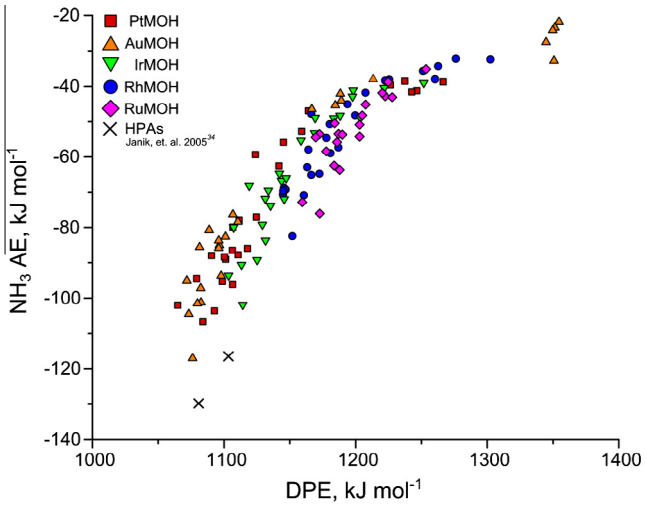

Fig. 4. Relationship between DPE and NH_3 AE.

characterization exists for ReO_x-promoted Pt or Ir. Thus, the observed increase in activity could be due to a change in the number of acid sites rather than a change in the acid strength of those sites.

In addition to ReO_x, MoO_x, and WO_x promoters that have been studied experimentally, RuO_x was also examined. Polyol hydrogenolysis over supported Ru has been shown to be highly active, although it is unselective due to Ru's affinity to break C–C bonds [4–6]. While this behavior is undesired for selective processes meant to maintain the skeletal carbon backbone in the production of chemical intermediates, other processes, such as reforming or hydrocracking, could potentially take advantage and benefit from ruthenium's ability to activate C–C bonds. An alloy that can utilize the hydrogenation abilities of Rh or Pt, coupled with the C–C hydrogenolysis abilities of Ru, could be improved if some of those Ru sites remained partially oxidized thus providing acid sites, similar to the other Re, W, and Mo promoters studied. The RuOH sites calculated here, however, were not as acidic as sites composed of other promoters, only decreasing the DPE of the base metal by an average of 63 kJ mol^{-1} for Ir, Pt, and Rh alloys, resulting in DPE values of 1120–1227 (average: 1176 kJ mol^{-1}), which may not be acidic enough to catalyze these reactions. Another approach would be to promote metallic Ru catalysts with ReO_x, MoO_x, or WO_x. This would utilize the ability of metallic Ru sites to break the C–C bonds, C–O bonds, and hydrogenate fragments while providing acid sites to aid in C–O hydrogenolysis.

ReO_x-promoted Ir shows the highest selectivity to *1,3-PDO* (>60% at low conversion) during glycerol hydrogenolysis [23], while the selectivity over ReO_x-promoted Pt is significantly lower (25–35%) [9]. The significant decrease in selectivity over the Pt alloy can be attributed to fact that the ReO_x-promoted Pt is predicted to be a stronger acid than ReO_x-promoted Ir, thus opening up additional reaction paths that will ultimately reduce its selectivity. It is also possible that metal sites in the alloy carry out hydrogenolysis chemistry along with the solid acid alloy sites. This would significantly lower the selectivity as unpromoted Pt is active in the hydrogenolysis of glycerol to the unselective *1,2-PDO* and propanol products and produces very little *1,3-PDO* [4,6,9]. Unpromoted Ir catalysts, however, are inactive for glycerol hydrogenolysis [18], indicating that hydrogenolysis on ReO_x-promoted Ir likely occurs only on the acid sites which are highly selective to 1,3-PDO formation.

Thus, if metal and acid sites of these promoted catalysts are active in carrying out hydrogenolysis, and metal-catalyzed hydrogenolysis is unselective compared to acid-catalyzed hydrogenolysis; then, suppression of metal-catalyzed hydrogenolysis should improve the selectivity. One method of suppression would be to choose a metal which is inactive for C–C or C–O bond hydrogenolysis. Au, which has a filled d-band, is a relatively inert metal which should only weakly interact with the alloyed metal promoter, thus allowing the alloyed promoter to interact more strongly with the oxygen of the hydroxide species and increase its acid strength. Promoted Au has the weakest O–H bonds (lowest DHE) of any of the alloys studied. The EA of Au systems is in between that of Rh and Ir consistent with experimentally reported WF measurements [36], which leads to DPE values on promoted Au surfaces that lie between 1072 and 1100 kJ mol^{-1} for the alloys with strong promoters (ReOH, MoOH, and WOH). The weak interaction of Au with the alloying metals, however, makes it unclear whether the synthesis of such alloys is feasible. In addition, it is not clear whether Au can effectively carry out the hydrogenation of the intermediates to complete the catalytic cycle, although this may present an advantage as it would result in the formation of unsaturated intermediates that could offer mechanistic insight into the process.

3.2. Adsorption of NH_3 to MOH^* Sites

NH_3 adsorption energies (AEs) reported in Table 1 range from 107 kJ mol^{-1} for PtReOH to 22 kJ mol^{-1} for monometallic AuOH. Fig. 4 shows the correlation between NH_3 AE and DPE and demonstrates that alloys of all four "bulk" metals follow a similar nonlinear relationship between the NH_3 AE and DPE over the wide range of DPE studied in this work. NH_3 AE increases rapidly with increasing DPE at first, indicating a nearly-linear relationship between DPE and NH_3 AE for strong acid sites which deprotonate, forming NH_4^+ (as further described in the SI, Figs. S7 and S8). At higher DPE values, the slope is lower, indicating a weaker trend for these systems, which do not deprotonate upon interaction with NH_3. For each "bulk" metal studied, this shift appears to occur at a different DPE and this inflection point correlates with the EA and WF of the bulk metal alloys (Pt > Ir > Au > Rh > Ru). Since DPE takes into account the EA, the shift in this inflection point may be coincidental. It appears that altering the base metal has a significant impact on the relationship between NH_3 adsorption and acid strength which prevents a direct 1:1 relationship between the NH_3 AE and the DPE of the system. NH_3 AE for phosphotungstic acid

($H_3PW_{12}O_{40}$, HPW) and phosphomolybdic acid ($H_3PMo_{12}O_{40}$, HPMo) reported by Janik et al. [37] are included for comparison and their DPE values are close to those calculated for the Pt- and Ir-based alloys, while their NH_3 AE are significantly stronger.

3.3. Ring-opening hydrogenolysis of HMTHF

Acid-catalyzed ring-opening hydrogenolysis of *HMTHF* on periodic (1 1 1) metal surfaces with a single MOH site was studied as shown in Fig. 5 for ReO_x-promoted Rh. Previous work [11] suggests the mechanism for this reaction proceeds via the combination of acid-catalyzed ring opening followed by subsequent hydrogenation of resulting unsaturated intermediates. Results show that *HMTHF* adsorbs to the acid site of the catalyst through the oxygen atom of the ring-ether which interacts with the bulk metal (Rh in Fig. 5) as well as with the hydroxide of the promoter (Re in Fig. 5). Upon adsorption, no proton transfer occurs between the ReOH and *HMTHF* due to its low proton affinity. The reaction proceeds by protonation of the ether group together with the ring opening of *HMTHF* and concomitant H-transfer from the carbon of the neighboring CH_2OH group to the activated carbon of the C–O bond as can be seen in comparing the reaction and transition states in Fig. 5 [11]. The concerted C–O activation and hydride transfer steps stabilize the carbenium ion transition state as we reported previously [11].

When the active site is ReOH embedded in a 4 × 4 Rh(1 1 1) surface, this mechanism results in an intrinsic activation barrier ($E_{Act,Int}$) of 83 kJ mol^{-1} and an overall apparent activation barrier ($E_{Act,Over}$) of 30 kJ mol^{-1} when the TS is referenced to *HMTHF* in the gas phase as shown in Fig. 5. On the (1 1 1) terrace site of a Rh_{201} particle, the intrinsic barrier is 88 kJ mol^{-1} and the overall barrier is 35 kJ mol^{-1}, which suggests that the much simpler surface model provides a reasonably good representation of (1 1 1) terrace sites on the 201 atom particle. We therefore used the ideal (1 1 1) surfaces to model the ring-opening reaction of *HMTHF* on a (1 1 1) terraces of ReO_x-, WO_x-, and MoO_x-promoted Ru, Rh, Ir, Pt, and Au catalysts as well as RuO_x-promoted Au and Pt surfaces.

The WF was calculated for the MO* structure for these surfaces to calculate the DPE^{WF} (Eq. (5)) due to the periodic nature of the crystal and the relatively small number of metal atoms in the calculation

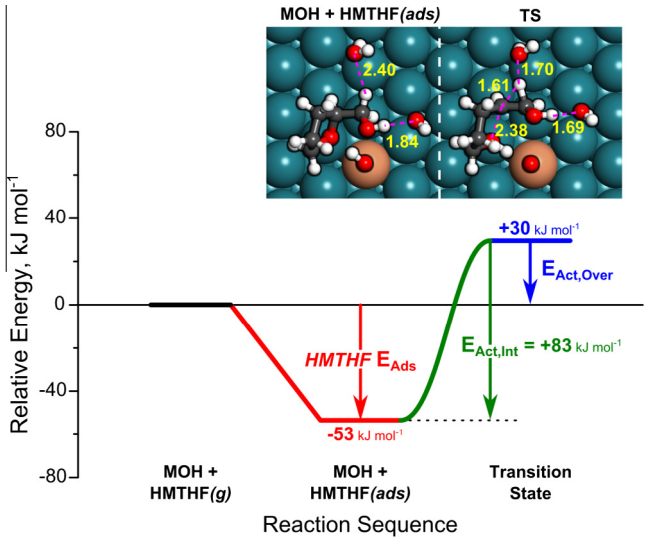

Fig. 5. Reaction profile for the activation of *HMTHF* at a ReOH site in a Rh (1 1 1) surface. Inset pictures show the top-down view of reactant and transition states. The reaction proceeds via a proton transfer from the hydroxide of the promoter to the oxygen in the ether together with the activation of the C–O bond at the more substituted tertiary carbon and concomitant hydride transfer from the α-CH_2OH group to the active carbon center [11].

(64). This WF for the periodic (1 1 1) surface is somewhat different than the WF calculated for the finite 201-atom particles, likely due to the differences in the electronic structure of the nm size and polycrystalline nature of the particles which have small band gaps verses the continuum of states for the periodic metal surface.

HMTHF adsorption energy has a weak relationship with the DPE^{WF} of the acid site, as shown in Fig. 6a, with a slope near 0.2 and an R^2 value near 0.75. In comparing the intrinsic or overall apparent activation barriers to the DPE of the acid site, stronger correlations are observed with slopes near 0.5 and 0.7, respectively and R^2 values near 0.9. These same values plotted against the NH_3 AE, shown in Fig. 6b, have similar correlations with slopes near 0.3, 0.7 and 1.0 and R^2 values above 0.8 for the *HMTHF* E_{Ads}, $E_{Act,Int}$, and $E_{Act,Over}$, respectively. If we compare the processes of NH_3 adsorption and *HMTHF* activation (referenced to the gas phase), we can see that these results indicate that the interaction energy between NH_4^+ and the MO^- conjugate base is very similar to the interaction energy between the positively charged TS and the MO^- conjugate base that results during the activation of *HMTHF*, as both measure the ion pair interaction strengths. It is important to note that such correlations between NH_3 AE and activation barriers or rates for acid-catalyzed reactions in zeolites have typically failed [28,38,39]. One issue for this correlation is the difficulties in measuring NH_3 AE through such methods as temperature-programmed desorption due to the presence of strong non-protonic binding sites on some materials and other issues outlined elsewhere [38,39]. Furthermore, accurate rate constants require an accurate accounting of Brønsted acid sites in the zeolite framework, which is non-trivial [38,39]. Similar issues arise even in comparing calculated adsorption energies and activation barriers as there very weak changes in the adsorption energies and other potential factors such as changes in the number of hydrogen bonds in examining the interaction with ammonia or basic probe molecule. The correlation is only present if the interaction between the NH_4^+ ion and the conjugate base is similar to the interaction between the positively charged transition state and the conjugate base. In zeolites, this is often not the case because of strong solvation effects between the positively charged transition state and the surrounding zeolite framework which may not be as prevalent in calculating the adsorption energies of the much smaller NH_4^+ cation that may not be as efficiently solvated [40]. If, as in the case of HPAs, NH_4^+ interacts through a bidentate mode with neighboring O atoms, an interaction that is not present in the transition state, then once again the changes in AE are unlikely to correlate with the changes in the activation barrier [37]. For the binfunctional MOx/M systems examined here, there are no strong solvation effects between the catalyst and the positively charged transition state or ammonium cation and the interactions between the conjugate base and the positively charged transition state and ammonium cation appear to be similar, thus resulting in the strong correlation observed.

If we examine the alloy compositions along with their overall activation barriers (Fig. 7), we note that promoted Pt alloys (neglecting PtRuOH) have the lowest overall apparent activation barriers with an average of 0 kJ mol^{-1}. WO_x-promoted Au has the lowest overall apparent barrier (-7 kJ mol^{-1}) of all of the systems, thus giving the promoted Au alloys the second lowest average value (8 kJ mol^{-1}) followed closely by promoted Ir (10 kJ mol^{-1}). Promoted Ru and Rh have significantly higher average barriers with 24 and 26 kJ mol^{-1}, respectively. Lastly, RuO_x-promoted Pt and Au have much higher activation barriers at 56 and 75 kJ mol^{-1}, respectively.

3.4. Effect of alloy structure

A range of other in-surface alloy compositions (Fig. 8) and atop-surface promoted systems (Fig. 9) were examined in addition to

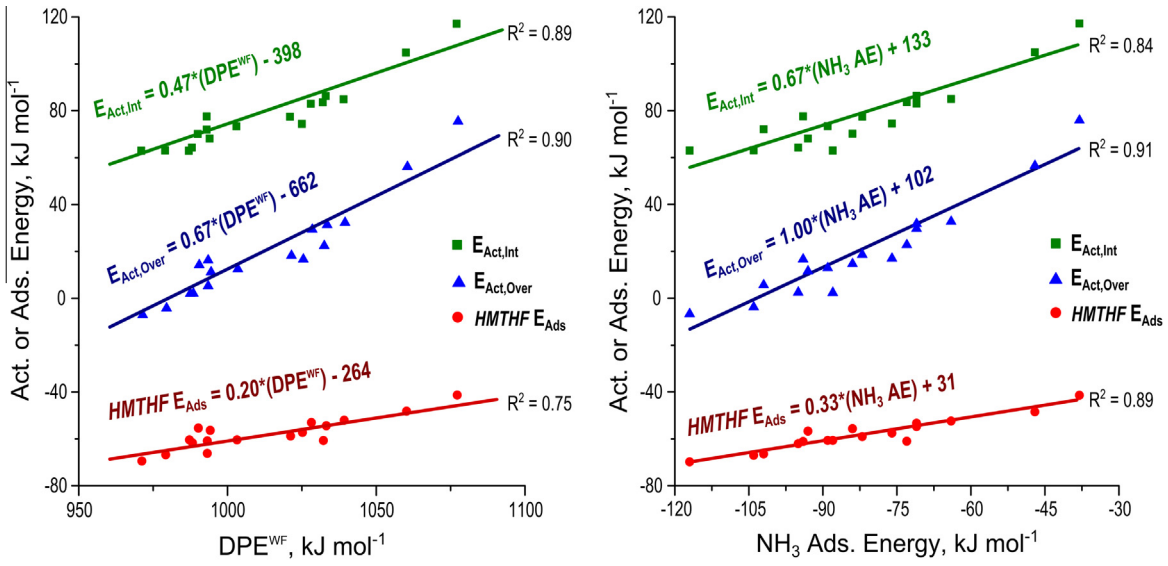

Fig. 6. The *HMTHF* adsorption energy (E_{Ads}) as well as the intrinsic ($E_{Act,Int}$) and overall apparent activation barriers ($E_{Act,Over}$) of the ring-opening reaction of *HMTHF* at MOH sites (M = Ru, Mo, Re, W) embedded in Ru, Rh, Pt and Au (1 1 1) metal surfaces plotted against the DPE of the MOH site (*A*, Left) or the NH_3 AE at that MOH site (*B*, Right). As shown in Fig. 5, the intrinsic activation barrier is referenced to HMTHF adsorbed at the MOH site and the overall activation barrier is referenced to HMTHF in the gas phase.

the in-surface monoalloy sites shown in Fig. 8a. Adding a neighboring in-surface ReO group to the monoalloy (Fig. 8b) decreases the acid strength of the Rh-ReOH site. The increase in the DPE relates to the decreased stabilization of the O* product state with the ReO neighbor and corresponding increase in DHE. If the neighboring site that is added is hydroxylated, as shown in Fig. 8c, a hydrogen bond can form between the vicinal OH* groups. This hydrogen bond is weakened following deprotonation at the highlighted position (Fig. 8c) due to ROH–ROH hydrogen bonds being stronger than OH—RO hydrogen bonds, thus increasing the DHE (and as a result, the DPE) of the acid site. This trend of increasing DPE continues as more neighboring Rh atoms are replaced with ReO or ReOH groups (Fig. 10a).

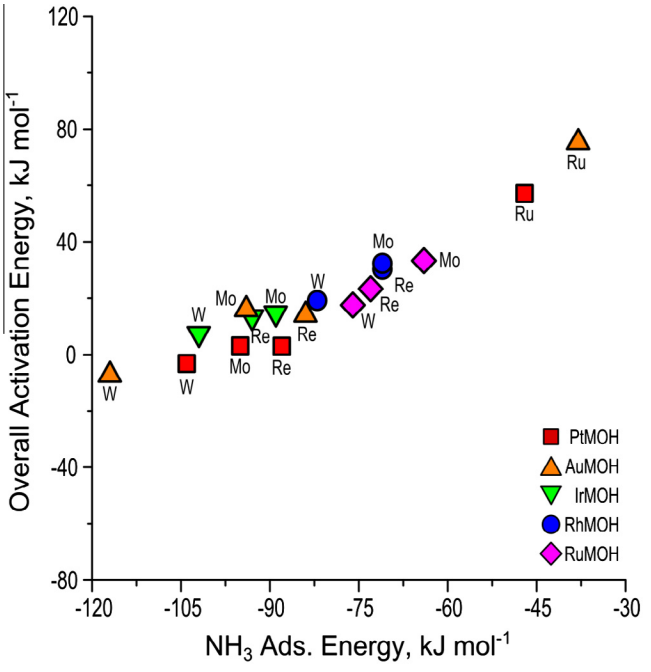

Fig. 7. The overall activation barrier of *HMTHF* at MOH sites (M = Ru, Mo, Re, W) embedded in Ru (♦), Rh (●), Pt (■) and Au (▲) (1 1 1) metal surfaces plotted against the NH_3 AE at that MOH site.

Rather than O* and OH* species binding atop to Re atoms, they can also bind three-fold to Re_3 sites. These sites can be three-fold fcc or hcp sites and can involve one or more uncoordinated edge or corner atoms, leading to 6 different possible configurations for the three Re atoms in the surface of the 201-atom nanoparticle. When the ensemble is made up three Re atoms (all with coordination numbers of 9) that form a three-fold fcc site within the (1 1 1) terrace (Fig. 8d), the DPE is 1125 kJ mol^{-1}, which is 20 kJ mol^{-1} more acidic than an atop OH* on a single Re atom (Fig. 8a). This is due to the decrease in DHE of 21 kJ mol^{-1} that results upon moving the OH from an atop single Re site to a three-fold Re fcc site.

In addition to the three-fold Re fcc site, OH can also form at the three-fold hcp site (Fig. 8e). The binding of O* at the three-fold Re hcp site (−613 kJ mol^{-1}) is more than 57 kJ mol^{-1} stronger than at the three-fold fcc site (−556 kJ mol^{-1}). The OH* BE, however, is weakened by 6 kJ mol^{-1} in moving from the three-fold fcc site (−306 kJ mol^{-1}) to the three-fold hcp site (−298 kJ mol^{-1}). The increase in the O* BE dominates over the weak changes in the OH BE, resulting in a very weak O–H bond with a DHE value of 130 kJ mol^{-1} and a DPE of 1060 kJ/mol, thus making this the site with the highest acid strength calculated on a ReO_x-promoted Rh particle.

The effects of coordination number are examined in Fig. 8f-i. Fig. 8f and g examine the binding energies, DHE and DPE for three-fold Re sites at less coordinatively saturated sites which contain two Re (1 1 1) terrace atoms and one edge atom for an average coordination number, $\overline{CN}$, of 8.33. The DPE of OH* bound in these sites are higher (lower acid strength) than the fully saturated fcc sites with $\overline{CN} = 9$. Fig 8h and i continue this trend, with three-fold sites consisting of one (1 1 1) terrace atom, one edge atom and one corner atom ($\overline{CN} = 7.33$) having lower acid strength as well. Decreasing the coordination number of the metal atoms involved in the three-fold site increases the O* BE, but this is offset by the greater increase in the OH* BE thus resulting in increases in the DHE and DPE. Therefore, the most active three-fold sites on a nanoparticle surface appear to be on coordinatively saturated (1 1 1) terraces of the Rh particles. Adding neighboring ReO* three-fold sites

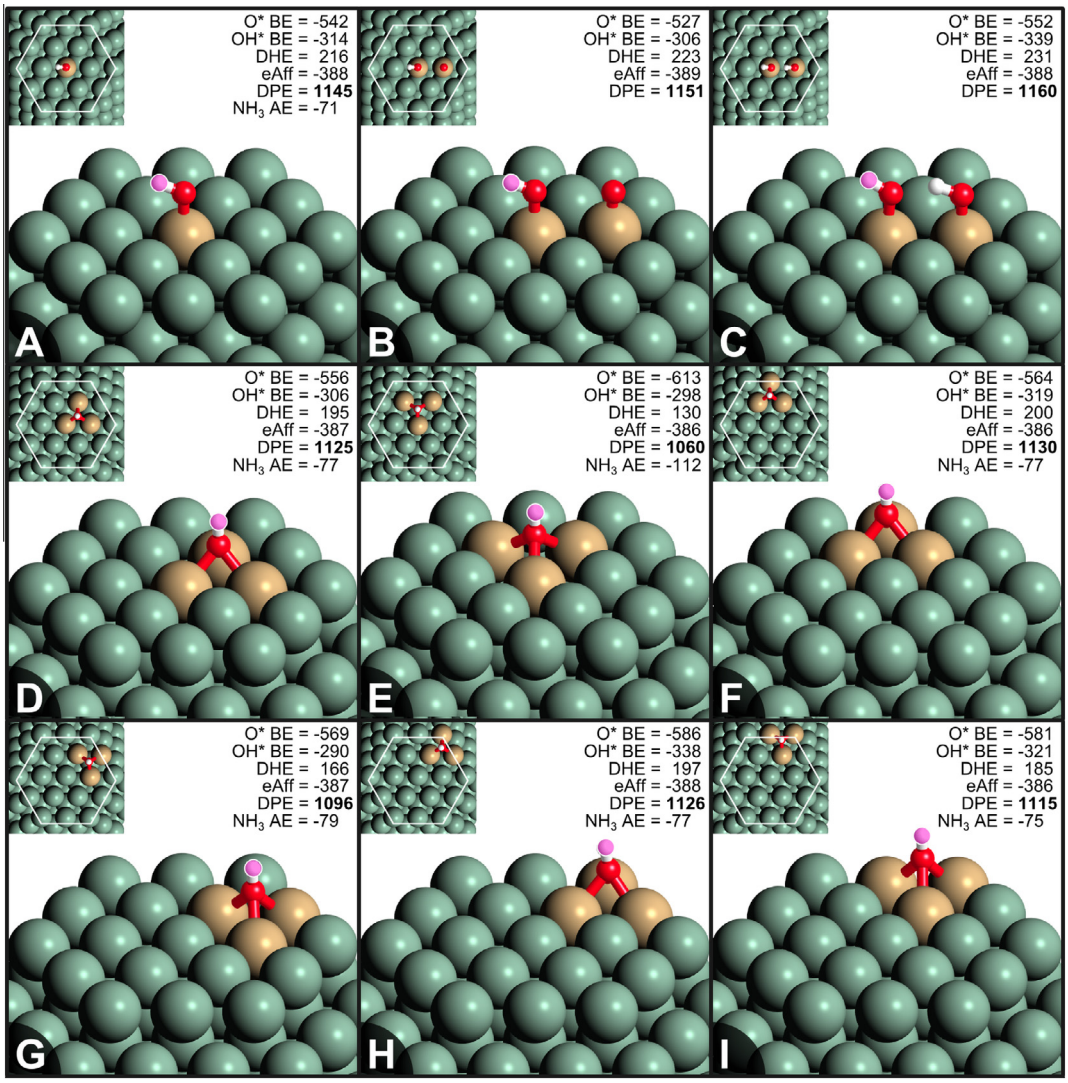

Fig. 8. The influence of Re surface composition on the DPE, DHE, EA, O^* and OH^* BE and NH_3 AE of in-surface Re-promoted Rh_{201} particles and their optimized structures.

has little effect on the DPE of the ReOH site as shown in Fig. 10b; however, the DPE does seem to decrease when neighboring Re_3OH sites are added (from 1125 to 1109 and 1103 kJ mol^{-1}, respectively). The final in-surface alloy site that was examined consists of OH^* bound to a four-fold hollow site on a (100) terrace shown in Fig. 9j. This site has similar characteristics to OH^* bound to a three-fold hcp site, in that it has a very strong O^* BE and a relatively weak OH^* BE, leading to a weak O–H bond with a DHE of 171 and a DPE of 1101 kJ mol^{-1}.

EXAFS has been performed on a number of these alloys, including Rh-ReO_x [10,13,21,26], Rh-MoO_x [21], Pt-ReO_x [9,27], and more recently, Ir-ReO_x [18]. Unfortunately, due to their proximity in the periodic table, the backscatter signals between the Rh–Mo, Pt–Re, and Ir–Re alloys cannot be fully resolved, limiting the amount of information one can draw from the EXAFS results. For Rh-ReO_x, however, it is possible to determine the Re–O, Re–Rh, Re–Re, Rh–Re, and Rh–Rh interactions and coordination numbers. While most of these coordination numbers vary with the Re:Rh loading, the Re–Rh CN remains constant, near 3.6 ± 0.8 [21]. This is not consistent with in-surface alloys, which would likely have Re–Rh CNs above 6. This is more consistent with Re atoms bound atop of the Rh surface, where they would interact with 3–4 Rh atoms, depending on whether it was above a (111) or (100) terrace of a Rh nanoparticle. The simplest such site is shown in Fig. 9k, in which a single Re atom sits in a three-fold fcc site of a Rh terrace. This Re atom has a CN = 3, as such the O^* BE is very strong (−655 kJ mol^{-1}), the strongest of any alloy calculated in this study and >100 kJ mol^{-1} stronger than when O^* is bound atop to a single Re atom *in* the Rh surface which has a CN = 9 (Fig. 15a). The OH^* BE is also very strong (−462 kJ mol^{-1}), however, which results in a fairly strong O–H bond with a DHE of 252 and a DPE of 1177 kJ mol^{-1}, higher than the DPE of the in-surface ReOH site (1145 kJ mol^{-1}, Fig. 15a).

Adding two neighboring Re atoms to create a three-fold OH^* on the above-surface Re atoms (Fig. 9l) weakens the O^* BE and OH^* BE to −634 and −369 kJ mol^{-1}, respectively, which results in a weaker and more acidic O–H bond than in the above-surface Re monomer (Fig. 9k), with a DHE of 180 kJ mol^{-1} and a DPE of 1112 kJ mol^{-1} (Fig. 9l). This above-surface alloy site is slightly more acidic than the in-surface alloy in which OH^* binds to a three-fold fcc site (Fig. 8d, 1125 kJ mol^{-1}). When the three Re atoms form a three-fold hcp site (Fig. 9m), the result is an increase in the O^* BE and OH^* BE and a net strengthening of the O–H bond, with a DHE of 198 kJ mol^{-1} and a less acidic OH^* site (DPE = 1129 kJ mol^{-1}). Unlike the previous case, this above-surface site is much less acidic than the corresponding in-surface site (Fig. 8e, 1060 kJ mol^{-1}). The acid strength increases from 1112 to 1106 kJ mol^{-1} for an additional ReO^* to 1091 kJ mol^{-1} for two additional ReO^* sites (Fig. 9n

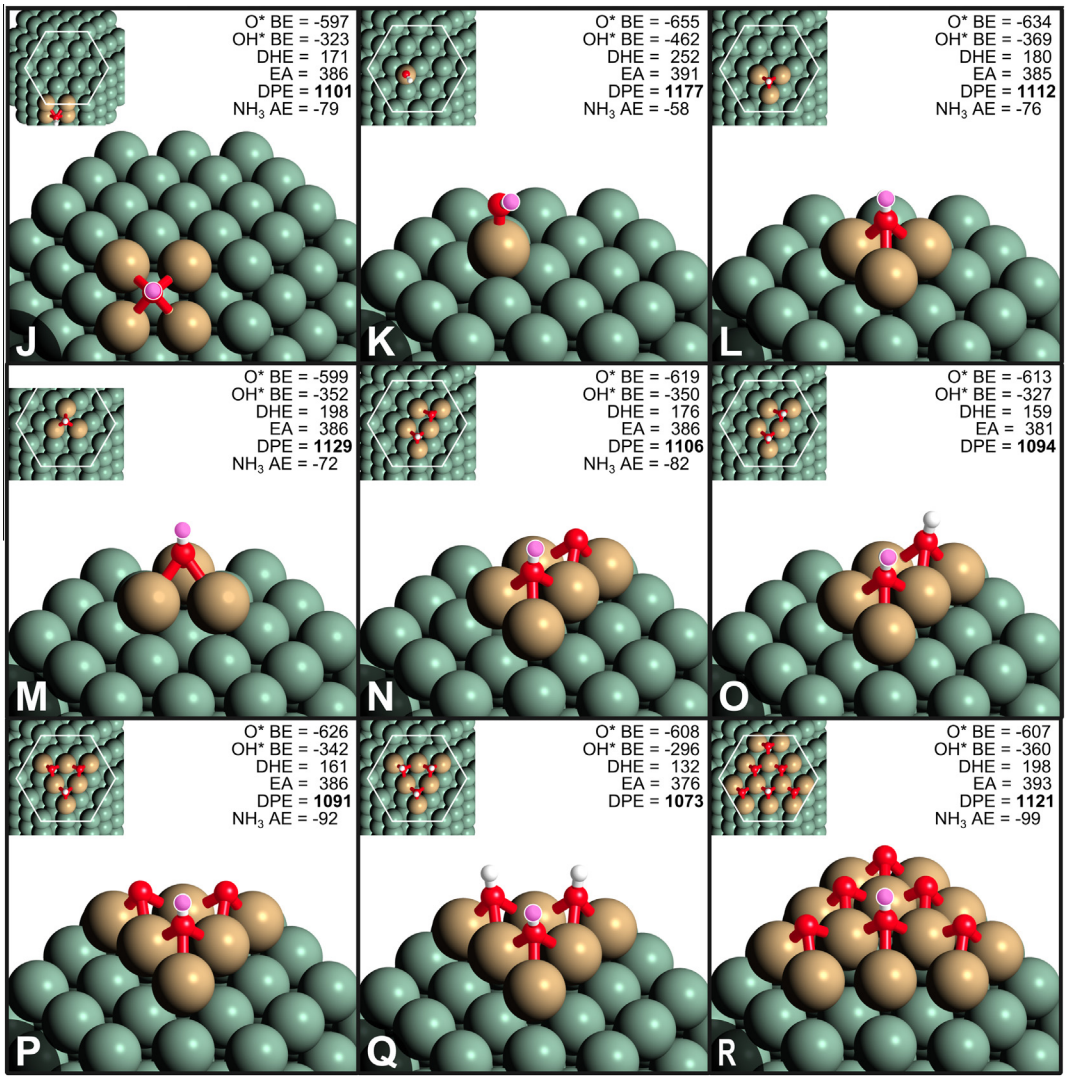

Fig. 9. The influence of atop-bound Re cluster size on the DPE, DHE, EA, O^* and OH^* BE and NH_3 AE of atop Re-promoted Rh_{201} particles and their optimized structures.

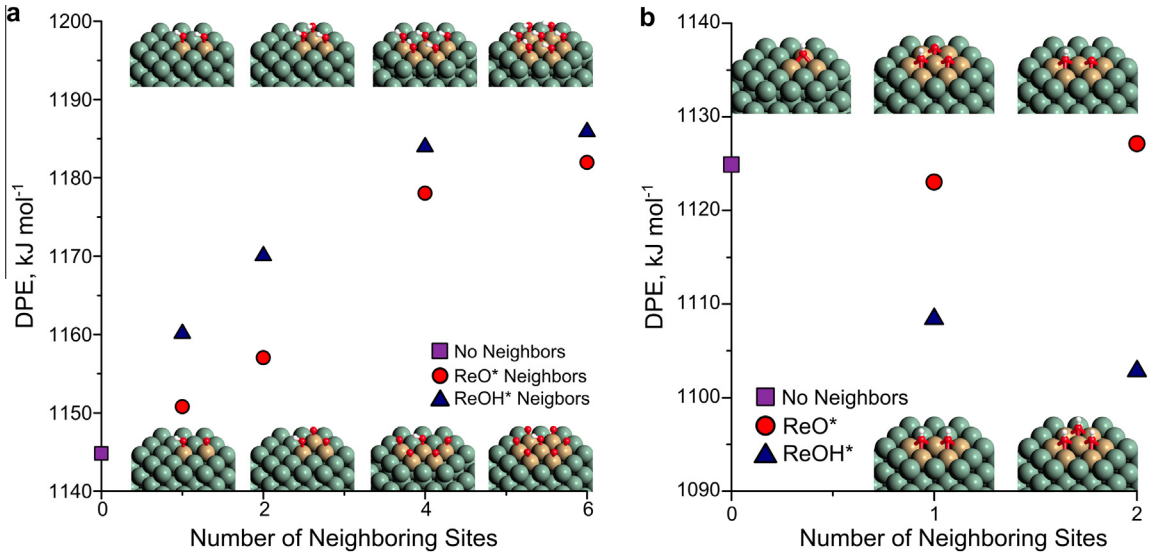

Fig. 10. (a) (Left) The effect of neighboring ReO^* or $ReOH^*$ sites on the DPE of in-surface ReO_x-promoted Rh clusters. (b) (Right) The effect of neighboring Re_3O^* or Re_3OH^* sites on the DPE of in-surface Re_3O_x-promoted Rh clusters.

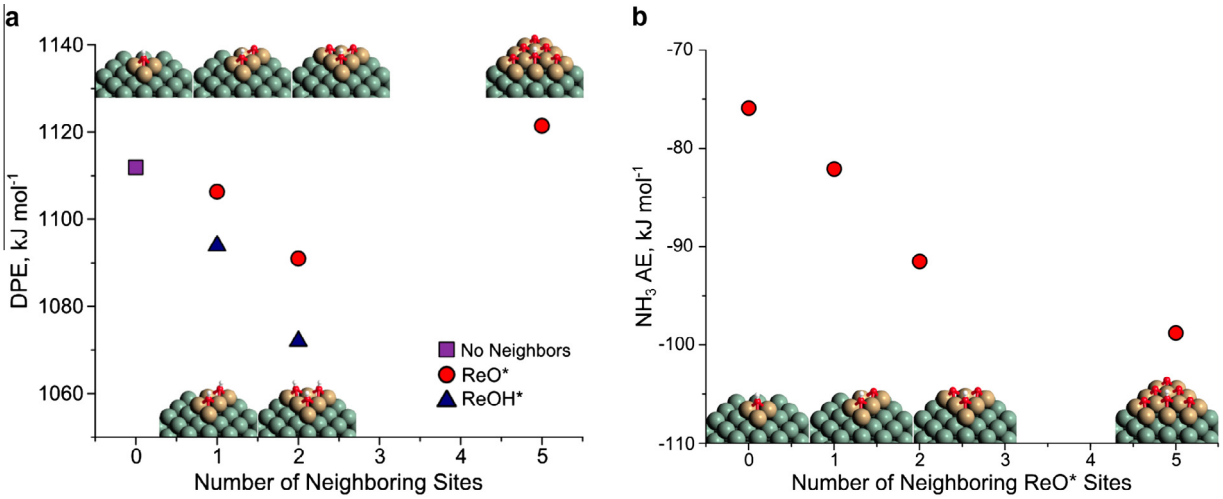

Fig. 11. (a) (Left) The effect of neighboring ReO* or ReOH* sites on the DPE of ReO_x-promoted Rh particles. (b) (Right) The effect of neighboring ReO* sites on the NH_3 AE of ReO_x-promoted Rh particles.

and p) and from 1112 to 1094 kJ mol^{-1} for an additional ReOH* and to 1073 kJ mol^{-1} for two additional ReOH* sites (Fig. 9o and q). This trend does not continue, however, to a larger ensemble of neighboring ReO* sites, as the alloy site shown in Fig. 16R has a DPE of 1123 kJ mol^{-1}. Interestingly, the NH_3 AE to these sites continue to increase through this large ensemble site as shown in Fig. 11.

In summary, OH* adsorbed atop a Re atom is a weaker acid than OH* adsorbed three-fold to three Re atoms, regardless of whether these Re atoms are in the surface of the Rh particle or sitting atop of the surface. If neighboring ReO* or ReOH* sites are present, the acid strength of OH* decreases when it is bound atop, partially due to the disruption of hydrogen bonds formed between vicinal ReOH and ReO sites. The acid strength of three-fold bound OH*, however, increases with the addition of neighboring Re_3O or Re_3-OH sites. Small Re clusters atop of the Rh particle are more consistent with previously reported EXAFS studies, which show Re–Rh CNs between 3–4 ± 1 and Re–Re CNs between 2–3 ± 2 depending on the Re:Rh loading [21]. Across all of these alloy structures, the EA remains fairly constant, even when the Re:Rh ratio becomes as high as 1:9 and the NH_3 AE continues to provide an additional metric of acid strength, which increases with decreasing DPE (Fig. 12).

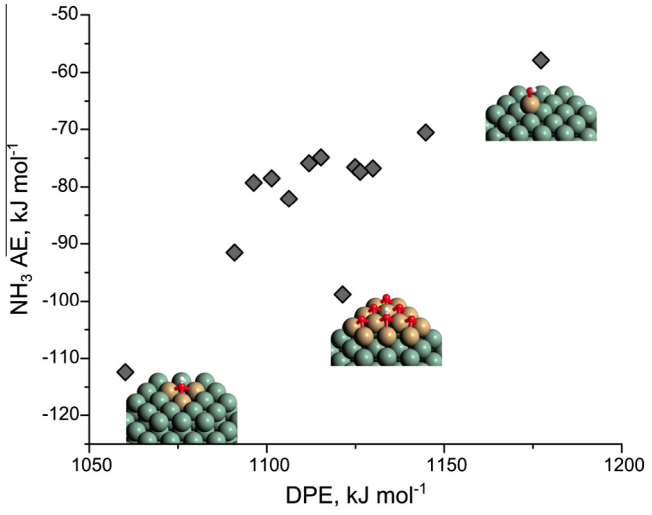

Fig. 12. The relationship between the NH_3 AE and DPE across a range of different ReO_x-promoted Rh structures.

4. Conclusions

Oxophilic MO_x promoters alloyed with noble metal catalysts yield Brønsted acid sites that enable acid-catalyzed hydrogenolysis reactions that are highly selective in the activation of C–O bonds with more substituted carbon centers. The ideal composition of these alloy sites combines an oxophilic metal from the left-hand side of the transition metal block in the periodic table (with Re and W providing the lowest DPE values) with a noble metal from the right side of the transition metal block, such as Rh, Ir, Pt, or Au. For reforming applications, the ability to activate C–C bonds may also be desired, suggesting the combination of an oxophilic metal promoter and a supported Ru catalyst.

The relationships between DPE, NH_3 AE and the ring-opening activation barriers for *HMTHF* were explored in detail in order to understand the influence of Brønsted acid strength on the adsorption properties of the OH sites on these different alloys and their role in catalyzing the activation C–O bonds of polyols. NH_3 AE at non-acidic hydroxides on pure surfaces such as Au is rather weak at ~25 kJ mol^{-1}. These energies increase linearly with the acid strength of the surface O–H group as measured by DPE with a slope of approximately 0.1 until a DPE of around 1200 kJ mol^{-1}, at which point there is an increase in the slope to ~0.4. This shift in sensitivity with DPE is related to a change between a hydrogen bonding interaction between NH_3 and the MOH site above a DPE of 1200 kJ mol-1 to a coulombic interaction between NH_4^+ and MO- which exists below a DPE of 1200 kJ mol^{-1}. More acidic sites show a large amount of scatter between the DPE and NH_3 AE which does not appear to be random, but instead appears to be related to changes in the EA of the bulk metal, which suggests that two MOH sites with identical DPE values can result in significantly different NH_3 AE due to differences in the local polarizability of the metal cluster rather than the bulk EA which is measured during calculation of the DPE.

Barriers for ring-opening activation of *HMTHF* decrease at more acidic MOH sites, as expected and due to the similarities of the activation of *HMTHF* and the adsorption of NH_3, a strong correlation is observed between the overall barrier and the NH_3 AE, indicating it may be a very good predictor of overall activity of an MOH site if it can be accurately measured from NH_3 TPD on these systems.

Calculated NH_3 AE and DPE values show distinct changes in the acid strength of alloy particles in which OH* binds at atop or three-fold sites and whether the MOH sites are embedded in the particle

surface or above the surface for ReO_x-promoted Rh catalysts. The results suggest that when the OH^* binds atop a single promoter metal, adding neighboring ReO and $ReOH^*$ intermediates result in hydrogen bonding interactions which are disrupted upon deprotonation, decreasing the acid strength; however, when OH^* binds three-fold to Re_3 sites, adding ReO^* or $ReOH^*$ neighbors decreases the DPE of the system, regardless of whether the Re atoms are in or on the surface of the Rh particle.

Overall, these systems represent unique embedded bifunctional solid acid/metal catalysts that are stable in aqueous conditions and capable of carrying out highly selective reactions on biomass-derived species, where it is often preferred to operate in liquid water. This work demonstrates how the acid strength of these systems changes with composition and structure as well as how the NH_3 AE and barriers for *HMTHF* hydrogenolysis change with acid strength.

Acknowledgments

The authors are grateful to the National Science Foundation for the financial support of this work under the NSF Award EEC-0813570 as part of the Center for Biorenewable Chemicals (CBiRC) at Iowa State University and the NSF award OISE 0730277 for the Partnership in International Research and Education (PIRE) and also kindly acknowledge access to the Molecular Science Computing Facility (MSCF) in the William R. Wiley Environmental Molecular Sciences Laboratory, a national scientific user facility sponsored by the U.S. Department of Energy, Office of Biological and Environmental Research at the Pacific Northwest National Laboratory. The authors also kindly acknowledge the very helpful discussions with Robert J. Davis (University of Virginia), Craig Plaisance (University of Virginia), James A. Dumesic (University of Wisconsin) and Mei Chia (University of Wisconsin).

Appendix A. Supplementary material

Supplementary data associated with this article can be found, in the online version, at http://dx.doi.org/10.1016/j.jcat.2014.03.016.

References

[1] A.J. Ragauskas, C.K. Williams, B.H. Davison, G. Britovsek, J. Cairney, C.a. Eckert, W.J. Frederick, J.P. Hallett, D.J. Leak, C.L. Liotta, J.R. Mielenz, R. Murphy, R. Templer, T. Tschaplinski, Science 311 (2006) 484.
[2] G.W. Huber, S. Iborra, A. Corma, Chem. Rev. 106 (2006) 4044.
[3] J.N. Chheda, G.W. Huber, J.A. Dumesic, Angew. Chem. 46 (2007) 7164.
[4] M.A. Dasari, P.-P. Kiatsimkul, W.R. Sutterlin, G.J. Suppes, Appl. Catal. A 281 (2005) 225.
[5] A. Brandner, K. Lehnert, A. Bienholz, M. Lucas, P. Claus, Top. Catal. 52 (2009) 278.
[6] E. Maris, W. Ketchie, M. Murayama, R. Davis, J. Catal. 251 (2007) 281.
[7] L. Ma, D. He, Top. Catal. 52 (2009) 834.
[8] J. Chaminand, L. aurent Djakovitch, P. Gallezot, P. Marion, C. Pinel, C. Rosier, Green Chem. 6 (2004) 359.
[9] O.M. Daniel, A. DeLaRiva, E.L. Kunkes, A.K. Datye, J.a. Dumesic, R.J. Davis, ChemCatChem 2 (2010) 1107.
[10] Y. Shinmi, S. Koso, T. Kubota, Y. Nakagawa, K. Tomishige, Appl. Catal. B 94 (2010) 318.
[11] M. Chia, Y.J. Pagán-Torres, D.D. Hibbitts, Q. Tan, H.N. Pham, A.K. Datye, M. Neurock, R.J. Davis, J.A. Dumesic, J. Am. Chem. Soc. 133 (2011) 12675.
[12] F.W. Lichtenthaler, Acc. Chem. Res. 35 (2002) 728.
[13] S. Koso, I. Furikado, A. Shimao, T. Miyazawa, K. Kunimori, K. Tomishige, Chem. Commun., 2009. p. 2035 (Cambridge, England).
[14] T. Miyazawa, Y. Kusunoki, K. Kunimori, K. Tomishige, J. Catal. 240 (2006) 213.
[15] Y. Kusunoki, T. Miyazawa, K. Kunimori, K. Tomishige, Catal. Commun. 6 (2005) 645.
[16] I. Furikado, T. Miyazawa, S. Koso, A. Shimao, K. Kunimori, K. Tomishige, Green Chem. 9 (2007) 582.
[17] S. Koso, Y. Nakagawa, K. Tomishige, J. Catal. 280 (2011) 221.
[18] Y. Amada, Y. Shinmi, S. Koso, T. Kubota, Y. Nakagawa, K. Tomishige, Appl. Catal. B 105 (2011) 117.
[19] L. Huang, Y. Zhu, H. Zheng, G. Ding, Y. Li, Catal. Lett. 131 (2009) 312.
[20] S. Koso, N. Ueda, Y. Shinmi, K. Okumura, T. Kizuka, K. Tomishige, J. Catal. 267 (2009) 89.
[21] S. Koso, H. Watanabe, K. Okumura, Y. Nakagawa, K. Tomishige, Appl. Catal. B 111–112 (2012) 27.
[22] A. Shimao, S. Koso, N. Ueda, Y. Shinmi, I. Furikado, K. Tomishige, Chem. Lett. 38 (2009) 540.
[23] Y. Nakagawa, Y. Shinmi, S. Koso, K. Tomishige, J. Catal. 272 (2010) 191.
[24] D.L. King, L. Zhang, G. Xia, A.M. Karim, D.J. Heldebrant, X. Wang, T. Peterson, Y. Wang, Appl. Catal. B 99 (2010) 206.
[25] L. Zhang, A.M. Karim, M.H. Engelhard, Z. Wei, D.L. King, Y. Wang, J. Catal. 287 (2012) 37.
[26] S. Koso, H. Watanabe, K. Okumura, Y. Nakagawa, K. Tomishige, J. Phys. Chem. C (2012).
[27] E. Kunkes, D. Simonetti, J. Dumesic, W. Pyrz, L. Murillo, J. Chen, D. Buttrey, J. Catal. 260 (2008) 164.
[28] M.J. Janik, J. Macht, E. Iglesia, M. Neurock, J. Phys. Chem. C 113 (2009) 1872.
[29] G. Kresse, J. Furthmuller, Comput. Mater. Sci. 6 (1996) 15.
[30] M. Methfessel, A. Paxton, Phys. Rev. B 40 (1989) 3616.
[31] P.E. Blochl, O. Jepsen, O.K. Andersen, Phys. Rev. B 49 (1994) 16223.
[32] J.P. Perdew, J.A. Chevary, S.H. Vosko, K.A. Jackson, M.R. Pederson, D.J. Singh, C. Fiolhais, Phys. Rev. B 46 (1992) 6671.
[33] G. Henkelman, H.A. Jonsson, J. Chem. Phys. 113 (2000) 9978.
[34] H.A. Jonsson, G. Mills, K.W. Jacobsen, Nudged Elastic Band Method for Finding Minimum Energy Paths of Transitions, World Scientific, 1998.
[35] G. Henkelman, H.A. Jonsson, J. Chem. Phys. 111 (1999) 7010.
[36] CRC Handbook of Chemistry and Physics version, 2008, pp. 12–114.
[37] M.J. Janik, R.J. Davis, M. Neurock, Catal. Today 105 (2005) 134.
[38] E. Shustorovich, H. Sellers, Surf. Sci. Rep. 31 (1998) 1.
[39] W.E. Farneth, R.J. Gorte, Chem. Rev. 95 (1995) 615.
[40] R.J. Gorte, Catal. Lett. 62 (1999) 1.